Research Article | Vol. 28, No. 26 / 21 December 2020 / Optics Express 39311
Optics EXPRESS

Long-distance fiber optic vibration sensing using convolutional neural networks as real-time denoisers

SASCHA LIEHR,[1,*] CHRISTOPHER BORCHARDT,[2] AND SVEN MÜNZENBERGER[2]

[1] Bundesanstalt für Materialforschung und -prüfung (BAM), Unter den Eichen 87, 12205 Berlin, Germany
[2] Bundesanstalt für Materialforschung und -prüfung (BAM), Unter den Eichen 87, 12205 Berlin, Germany
[*] sascha.liehr.ofs@gmail.com

Abstract: A long distance range over tens of kilometers is a prerequisite for a wide range of distributed fiber optic vibration sensing applications. We significantly extend the attenuation-limited distance range by making use of the multidimensionality of distributed Rayleigh backscatter data: Using the wavelength-scanning coherent optical time domain reflectometry (WS-COTDR) technique, backscatter data is measured along the distance and optical frequency dimensions. In this work, we develop, train, and test deep convolutional neural networks (CNNs) for fast denoising of these two-dimensional backscattering results. The very compact and efficient CNN denoiser "DnOTDR" outperforms state-of-the-art image denoising algorithms for this task and enables denoising data rates of 1.2 GB/s in real time. We demonstrate that, using the CNN denoiser, the quantitative strain measurement with nm/m resolution can be conducted with up to 100 km distance without the use of backscatter-enhanced fibers or distributed Raman or Brillouin amplification.

1. Introduction

Distributed acoustic sensing (DAS), or distributed vibration sensing (DVS), in optical fibers has experienced a steep increase in research and application in recent years. This technique allows for dynamic strain measurement along an optical fiber, typically with nε (nm/m) resolution. It is now being used for a wide range of applications [1] from the oil and gas sector, security and perimeter monitoring, seismic applications, traffic monitoring, to structural health monitoring. Most measurement principles use Rayleigh backscattering signals in combination with coherent optical pulse reflectometry for high-sensitivity strain change measurement [2]. They are commonly based on demodulation of local interference changes along the fiber and are often referred to as phase-sensitive optical time domain reflectometers (OTDR), or φ-OTDR. For various applications, a long distance range over tens of kilometers is required. This is specifically important if a single DAS system must cover sensor lengths up to 100 km, as it is for example the case for the measurement along sub-sea power line cables [3]. The very low signal-to-noise ratio (SNR) of distant backscatter signals eventually limits the maximum distance range of the sensor system.

Various techniques have been proposed to overcome these attenuation-limited distance boundaries: Hardware-supported distance range extensions are, for example, achieved by distributed Raman and/or Brillouin amplification [4–6], or using remotely pumped Erbium-doped fiber amplifiers (EDFAs) [7]. Another approach to increase the distance range and locally boost the SNR is to increase the Rayleigh backscattering signal power by enhancing the backscatter coefficient of the fiber by inscribing continuous [8] or random [9] weak fiber Bragg gratings. Such special backscatter-enhanced fibers connected to the distant end of low-loss section have, for example, been used to increase the backscatter signal locally [10] and detect strain signals

#402789 https://doi.org/10.1364/OE.402789
Journal © 2020 Received 28 Jul 2020; revised 2 Nov 2020; accepted 11 Nov 2020; published 14 Dec 2020

Optics EXPRESS

at more than 112 km distance. Increased attenuation of high-scattering fibers, however, makes this solution only viable for a reduced distance range. Similarly, the inscription of scattering dots [3,11] or weak fiber Bragg gratings [12,13] can also boost the local signal power at the cost of increased fiber attenuation. For a wide range of applications, the installation of additional hardware, such as remote amplifiers, pump lasers, or costly backscatter-enhanced fibers is not feasible.

In this work, we develop advanced signal processing techniques to boost the SNR of raw Rayleigh backscatter data prior to computing DAS strain data from the denoised results. We deploy deep learning methods and develop convolutional neural networks (CNNs) to denoise two-dimensional Rayleigh backscatter signals from standard single-mode optical fibers. We use the wavelength-scanning coherent optical time domain reflectometry (WS-COTDR) technique [14] to sample two-dimensional raw backscatter data along the fiber distance coordinate and the optical frequency coordinate. As opposed to previously proposed 2D filtering methods, we apply deep learning methods and restore extremely noisy backscatter signatures in the fiber distance – optical frequency plane. In our second step, the strain signals are computed from the denoised data and analyzed to quantify the denoising performance [15].

Our objective is to optimize the sensor performance for long distance measurement at the presence of very high noise. We solely explore the impact and possibilities of artificial neural network (ANN)-based raw data processing to extend the distance range and improve the strain SNR. No additional in-line signal amplification, distributed amplification, or Rayleigh backscatter enhancement is deployed. Real-time analysis of data-intensive DAS results is a general challenge [16]. Our focus is therefore not only on raw data denoising performance, but with equal importance, on minimizing the computation time in order to achieve real-time denoising capabilities for distributed vibration sensing using WS-COTDR.

In general, filtering [17,18] and denoising of raw signals play an important role in fiber optic sensor applications. With the emergence of distributed fiber sensing, and multi-dimensional data sampling, more complex data processing algorithms have been developed and deployed. Raw data denoising of multi-dimensional fiber optic sensor signals using classic non-ANN methods, such as non-local means [19] and constrained least squares filtering [20] showed significant performance improvement for noisy distributed Brillouin and Raman spectra. Two-dimensional filtering of DAS signals along the time and distance axes has been proposed to increase the SNR of the vibration signal. These algorithms include curvelet denoising algorithms [21], two-dimensional edge detection [22], and adaptive two-dimensional bilateral filtering [23]. The multi-dimensionality of sensor data as well as the complexity and interdependency of the physical effects in the optical fiber suggests that machine learning techniques more particularly ANNs could extract even more details. Although deep learning and artificial neural networks are widely used in photonics [24], relatively few works have been presented that target optical fiber sensor raw data. For clarification: We define raw data processing either as a preprocessing step to extract more information prior to computing the actual measurand (for example strain) or as computation of the measurand directly from raw data. ANN processing of Brillouin raw data spectra proved advantageous for temperature prediction [25–30], and for strain-temperature discrimination [31,32]. It was also demonstrated that CNNs designed for general image denoising can improve the sensing performance of 2D raw Raman OTDR data [33]. For DAS data, however, the focus of research on ANNs is almost exclusively on the post-processing of strain data for event recognition and event classification [34–45]. To the best of our knowledge, denoising of DAS raw data using deep learning techniques has not yet been demonstrated. Only neural network-based DAS raw data processing has been proposed for strain prediction from Rayleigh backscatter spectra with improved resolution and noise tolerance [15]. These results also demonstrated that ANN-based processing can significantly reduce computation time and qualify data-intensive

Optics EXPRESS

DAS data processing for real-time applications. This technique is also used here to predict strain data from denoised data.

The remainder of this paper is structured as follows. The WS-COTDR measurement principle and experimental setup are introduced in section 2.1. The specific denoising task and evaluation method are further explained in section 2.2. Training data generation, the final neural network architecture, and parameter search are summarized in section 3. Two different CNN denoising models are tested on measurement data, and are compared to the state-of-the-art block matching denoising algorithm BM3D [46] in section 4. The results and implications are discussed in section 5 and concluded in section 6.

2. Measurement principle and specific denoising problem

2.1. Experimental setup (WS-COTDR)

We recently proposed the wavelength-scanning COTDR technique for dynamic and high strain resolution measurement along standard single-mode optical fibers [14]. Using this technique, sequences of coherent optical pulses with increasing pulse optical frequencies within each sequence are repeatedly sent into the fiber under test (FUT). Incremental wavelength steps (frequency shifts $\Delta\nu$) during each pulse sequence are realized by direct laser current modulation of a continuous wave laser source using a sawtooth periodic signal, see Fig. 1(a).

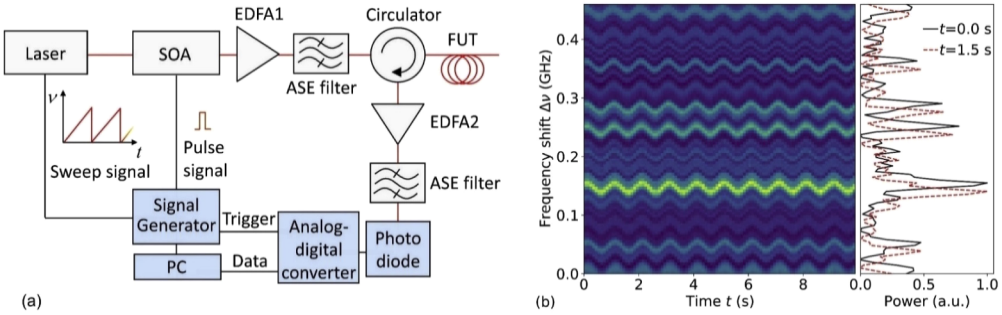

Fig. 1. WS-COTDR setup with semiconductor optical amplifier (SOA) for pulse generation, erbium-doped optical amplifiers (EDFAs) for pulse and backscatter signal amplification, and amplified spontaneous emission (ASE) filters. (b) Example of measured backscatter spectra for one distance sample during harmonic modulation, recorded with measurement settings used in this paper. The measured frequency shift of the spectrum is proportional to strain change [14].

During each laser wavelength sweep (or respective frequency sweep), up to 100 pulses of known optical frequencies are sequentially sent into the FUT. The Rayleigh backscattered light is individually sampled by an analog-to-digital converter (ADC) for each pulse frequency as a function of distance with 500 MS/s (about 20.4 cm sampling resolution) and 14 bit resolution. This way, a distributed Rayleigh backscatter spectrum is repeatedly measured along the FUT. We record backscatter amplitudes in the three dimensions: distance, optical frequency, and time. Any change of temperature or strain distribution along the fiber causes a proportional frequency shift of the local Rayleigh backscatter spectra [14], see Fig. 1(b). A strain change distribution over distance and time can thus be obtained by computing these frequency shifts relative to a reference sweep result for each spatial sampling point along the fiber. The difference to most pulse reflectometry DAS approaches is that strain changes are computed from frequency shifts of Rayleigh backscatter signatures instead of tracking and unwrapping interferometric phase changes from single wavelength backscatter results. The WS-COTDR technique requires to measure multiple backscatter traces per strain result, but it has the significant advantage that

Optics EXPRESS

it is a true reference-based method. That means that recorded reference backscatter spectra can be stored and reused to compute relative strain changes at any time. As opposed to typical phase-tracking approaches, WS-COTDR measurements can be interrupted and resumed without loss of reference.

The laser sweep rate during a measurement is typically in the kHz range and several thousands of spatial Rayleigh spectra must be compared for each sweep. Therefore, the computational effort is immense. In order to conduct these computations in real-time, specifically trained artificial neural networks (ANNs) have been developed for strain prediction from raw sweep data [15]. The use of ANNs not only improved the strain resolution, but also decreased the computation time by more than two orders of magnitude in order to be used for real-time strain measurement. This ANN-based strain computation approach from Rayleigh spectra is also used on the denoised results in this work.

The WS-COTDR technique and measurement setup shown in Fig. 1(a) are described in more detail in Ref. [14]. Notable changes from the previous implementation are the narrow-bandwidth ASE filters (3 GHz after EDFA1, and 1.5 GHz after EDFA2), and a laser source with reduced linewidth of 1.5 kHz. Pulses of 100 ns duration (resulting in 10 m spatial resolution) are sent into a 100.1 km long FUT (Corning SMF-28 ULL with 0.161 dB/km attenuation and a Rayleigh backscatter coefficient of −82 dB at 1550 nm for 1 ns pulse duration). The performance of the denoisers was tested at different fiber distances using the measurement settings of: 100 ns pulse duration (10 m spatial resolution), 1 kHz pulse repetition rate, and a laser frequency sweep rate of 10 Hz.

A change of the laser central wavelength has proportional influence on the measured shift of the backscatter spectrum [see Fig. 1(b)] as a physical strain change of the fiber itself [14]. In order to induce a strain-equivalent shift of the backscatter spectrum along the fiber, we superimposed an additional low-amplitude sinusoidal laser current modulation onto the sweep-modulated laser current. This results in a uniform and reproducible strain-equivalent backscatter signal shift in the frequency axis over the length of the fiber. This way, the denoising performance during a strain-equivalent frequency shift modulation can be easily tested at arbitrary fiber distances. Unwinding the fiber spools and cutting the fiber at multiple distances to insert a piezo stretcher is not necessary.

2.2. Denoising problem and training approach

Three-dimensional backscatter data is recorded along the axes: distance, optical frequency, and time. The distance-frequency plane exhibits characteristic backscatter signatures with shapes and statistical distribution independent of fiber distance and strain. The convolutional 2D denoising models are therefore optimized, trained and tested in the distance-frequency plane.

The performance of general 2D image denoising methods using ANNs, and especially CNNs, has shown rapid advancement in recent years [47]. CNNs have the potential to out-perform nonlocal self-similarity models such as BM3D, also for non-photographic image applications.

One of the most important advantages of ANN-approaches is the potentially low computation time. In contrast to many other denoising algorithms where a rather expensive optimization computation must be conducted for every new image, the optimization of an ANN is only conducted during the training phase. The prediction (inference) of denoised images from noisy images is then conducted by the optimized ANN model. This is efficiently achieved by a series of matrix multiplications followed by elementwise non-linear transforms on graphics processing units (GPUs), and can reduce inference times by orders of magnitude. However, most of the proposed methods rely on careful parameter setting, are computationally expensive, or require specific models for specific denoising tasks or noise levels [48]. More recent architectures do not rely on knowledge about the noise level of the image and are referred to as a blind denoisers [49]. Most general image denoisers target arbitrary photographic color images that contain three color

Optics EXPRESS

channels (RGB). Our task is to conduct blind denoising of single channel (grayscale) images with 16 bit resolution. Our data-intensive application requires to process a steady data stream in the order of several hundreds of MB/s.

We use supervised learning in this work: A function is learned that maps our input data to the output data by learning from examples of input-output image pairs. In our specific case, we train CNNs to predict denoised 2D data from noisy 2D input data. CNNs typically consist of an input layer, multiple convolutional hidden layers, and an output layer. The convolutional layers compute the sliding dot product of the output of the previous layer and a number of learnable kernels (or filters). Thereafter, a nonlinear activation function, such as rectified linear unit (ReLU), is applied before the result is passed to the next layer. During the initial training phase of the network, the CNN is presented with noisy 2D input data Y. The weights of the individual filters are adjusted during each training epoch to minimize a loss function, i.e. the deviation of the CNN output to the corresponding "clean", or ground truth, images X. The aim of the trained denoiser is to recover a clean image $x \in X$ from a noisy image $y \in Y$. A noisy image y can be described as a superposition of ground truth images x with noise n as $y = x + n$. The noise n is often modelled as additive white Gaussian noise (AWGN) with a standard deviation of σ.

General purpose image denoisers have to be able to denoise any structure and structural distributions in the images and "have to compromise" for high-frequency signals as well as extended uniform structures. In our application, however, the prevailing structural patterns in the images exhibit a specific shape, size, orientation, and distribution, see Fig. 2(a). These characteristic patterns owe from interference of multiple Rayleigh scatterers within the length of the pulse that propagates along the fiber. The statistic distribution of shapes, sizes, and aspect ratios of these structures are a function of the optical pulse duration, the frequency sweep step size, the sampling rate, and the detection bandwidth. Since the characteristic structures have a relatively high aspect ratio, and prevailing orientation along the distance axis, we also explore using filters with matching aspect ratios. We presumed that matching the filter size (or shape) to the characteristic structures, and matching the receptive field to the structure size and orientation will reduce the necessary depth of the CNN and, therefore, necessary number of convolutional layers of the denoiser.

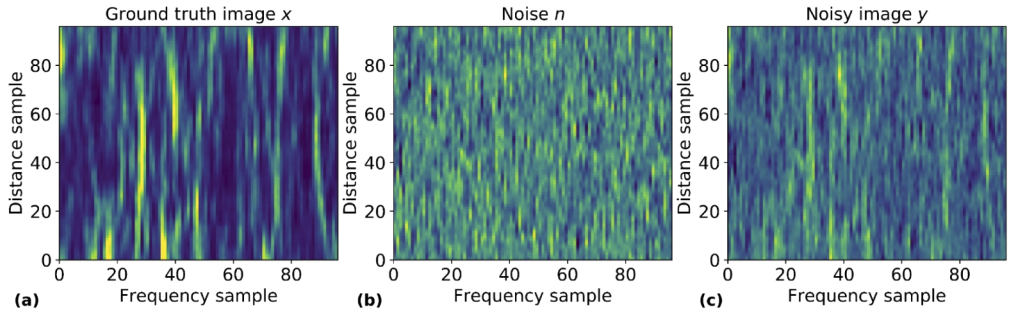

Fig. 2. (a) Ground truth image x (measured WS-COTDR spectrum vs. distance), (b) measured noise distribution image n, and (c) noisy image y (x superimposed by noise n with noise factor of 1). The size of the single image is 96 frequency samples by 96 distance samples.

Another difference to general image denoising applications is that the noise exhibits distinct spatial patterns, see the measured 2D noise distribution in Fig. 2(b). Due to the small bandwidth of the transimpedance amplifier of the photodetector module (35 MHz) in comparison to the (spatial) sampling rate of the analog-to-digital converter (500 MS/s and 250 MHz analog bandwidth), the detector noise is low-pass filtered and spreads over several distance samples. Neighboring

Optics EXPRESS

noise "pixels" along the frequency axis are however uncorrelated. The histogram of all noise amplitudes (all pixels) follows a Gaussian distribution.

Due to the very specific distribution and orientation of the backscatter structures as well as the spatial structure of the noise, it could be expected that a deep learning approach would have advantages to restore these patterns in the presence of severe noise. The image size for a single denoising operation (input size and output size of the denoiser) is 96×96 pixels. For a denoising operation of a distributed measurement over several kilometers, multiple 96×96 images along the fiber distance are denoised and stitched along the distance axis for each frequency sweep result.

A commonly used measure to quantify the denoising performance of an algorithm is the peak signal to noise ratio (PSNR). This quantitative pixel-wise measure is, however, not always the best method to determine the overall denoising performance [50]. Also perception-based models such as the structural similarity index measure (SSIM) [51] are not the most valid choice for our purpose. Since our application requires to compute accurate strain signals from denoised data, we defined our own application-specific performance measures: We aim to minimize the amplitude spectral density (ASD) noise of the computed strain results, and maximize the accuracy of the strain modulation amplitude [14], see also Fig. 3(b). These decisive performance criteria are evaluated on actual noisy measurement data recorded at different distances along the fiber. Figure 3(a) shows exemplarily sinusoidal strain signals over time for a single sampling position at 90.034 km distance, computed from noisy measurement data and denoised measurement data, respectively. As indicated in Fig. 3(b), the strain modulation amplitude, as well as the strain ASD noise (square root of the signal power spectral density [52]) above the modulation frequency is obtained from the frequency domain results.

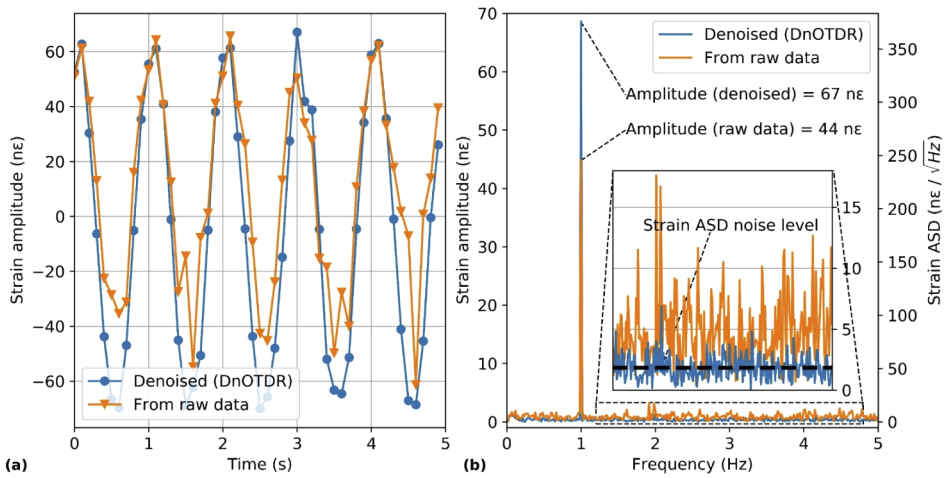

Fig. 3. Example of sinusoidal strain results during a 1 Hz harmonic modulation equivalent to 67 nε at 90.034 km distance: (a) Computed strain results from raw data, and from denoised result using CNN denoiser DnOTDR (introduced in section 3). (b) Frequency domain spectrum of the strain result computed from raw data and denoised data (magnified inset with indication for strain ASD noise level).

3. Data generation and training

Our procedure for the generation of training data is to independently measure a low-noise ground truth dataset X, and a noise dataset N. Examples for single images $x \in X$ and $n \in N$ are shown in Fig. 2(a) and Fig. 2(b), respectively. The noisy training dataset Y is then generated by

Optics EXPRESS

superimposing the ground truth dataset X with the measured noise dataset N. Details on data generation and training of the CNNs are summarized in the following subsections.

3.1. Training data generation

All training data was obtained from measurement data: The **ground truth dataset** $\boldsymbol{X}$ was generated by conducting low-noise WS-COTDR measurements over fiber lengths up to 7 km. The ground truth dataset exhibits insignificant label noise since the SNR is high for such short fiber distances. The same measurement settings as during the recording of the noisy long-distance test dataset were used. Only the laser current of the EDFA2 was reduced not to exceed the ADC input range. We sampled ground truth data from the same fiber during wavelength scans at 12 different laser central frequencies. Sufficient spectral separation between the individual wavelength scans was maintained to prevent spectral overlap of the different sweeps. This way uncorrelated 2D backscatter signatures along the distance and laser frequency dimensions were generated. 100 different pulse optical frequencies were sent into the fiber during each laser frequency sweep. The first four pulses of the sequence are within the falling edge of the laser frequency modulation and were discarded [14]. Each Rayleigh backscatter spectrum therefore consist of 96 optical frequencies. Individual 96×96-pixel images [see Fig. 2(a)] were extracted from the measured 2D Rayleigh data. A spatial overlap of 64 distance samples was chosen to increase the number of training images. The 64008 images of the ground truth dataset X were sampled during an additional sinusoidal 2 Hz laser frequency modulation. This was done to also include images with distorted structures to the training dataset and improve the model's generalization capability with respect to varying strain signals and amplitudes.

The 64008 independent 96×96 images of the **noise dataset** $\boldsymbol{N}$ [see Fig. 2(b)] were recorded by only sampling the low-pass filtered photodetector noise signal. The same measurement settings (high EDFA2 current of 80 mA) as during the recording of the long-distance test dataset were used but without a fiber connected to the measurement setup. This way, noise amplitudes similar to the actual long-distance measurement were generated.

The **noisy dataset** $\boldsymbol{Y}$ was obtained by adding the noise data N to the ground truth data X. Before superimposing noise N and ground truth X, each individual image of both datasets was z-score standardized, resulting in zero mean and a standard deviation of one for each image. Before adding and noise data N to the ground truth data X, the noise dataset was multiplied by a factor (noise factor). This noise factor was treated as a hyperparameter during the training of the models in section 3.4.

3.2. Validation data generation

After each training epoch, the model's performance was validated on a measured strain signal. The current denoising model was validated with respect to the computed strain results (strain ASD noise and strain amplitude) on a long-distance backscatter validation dataset. This validation dataset was measured over 20 seconds at 100 km distance during a 2 Hz modulation with a strain-equivalent amplitude of 64 nε. More details of the validation approach are given in section 3.4.

3.3. Test data generation

The denoising CNNs are tested on measurement data. The test dataset was sampled at multiple fiber distances $z_0 = \{60\text{ km}, 70\text{ km}, 80\text{ km}, 90\text{ km}, 100\text{ km}\}$. Starting at each position z_0, about 80 m long fiber sections were sampled for 60 seconds during a strain-equivalent modulation amplitude of 67 nε at 1 Hz, respectively. We evaluated the denoising performance on this test dataset with respect to strain ASD noise and strain amplitude. The results are presented in section 4.

Optics EXPRESS

3.4. Model architecture, hyperparameter testing, and training

The input images for our application differ significantly from the typical input images of general-purpose photographic image denoisers with respect to the image content, noise shape, as well as the extremely high level of noise. We explored combinations and alterations of numerous state-of-the-art deep convolutional image denoiser architectures for this specific task. This included convolutional denoising auto-encoders, and models with residual noise subtraction or skip connections. Particularly, various properties of the CNN denoisers DnCNN [49], and FFDNet [53] proved advantageous. We conducted a wide hyperparameter search to optimize the denoising performance with respect to the correct modulation signal amplitude, minimum strain ASD noise, and minimum computation time.

We optimized the following model hyperparameters: The use of a residual layer for noise subtraction [49], down-and-up conversion layers [53], noise maps [53], the number of convolutional layers, the use of batch normalization layers, the number of convolutional layers, the number of filters per layer, the type of activation function (rectified linear unit ReLU, exponential linear unit ELU, and tanh), and the shape of the 2D filters. The following training parameters were tuned: learning rate, training batch size, and the noise factor. As loss functions, mean squared error (MSE), and negative Pearson correlation coefficient (NPCC) were explored. The ADAM optimizer [54,55] was used for all training settings.

Two different CNN architectures were identified as most promising and were optimized and tested for long-distance raw data denoising performance: The first architecture is a residual denoiser and has similarity to the DnCNN architecture [49]. In the following, it is referred to as **DnCNN***. The second convolutional denoiser features a "down-und-up" sampling functionality [53] and is referred to as **DnOTDR**. The two CNN denoising architectures used in this work are depicted in Fig. 4.

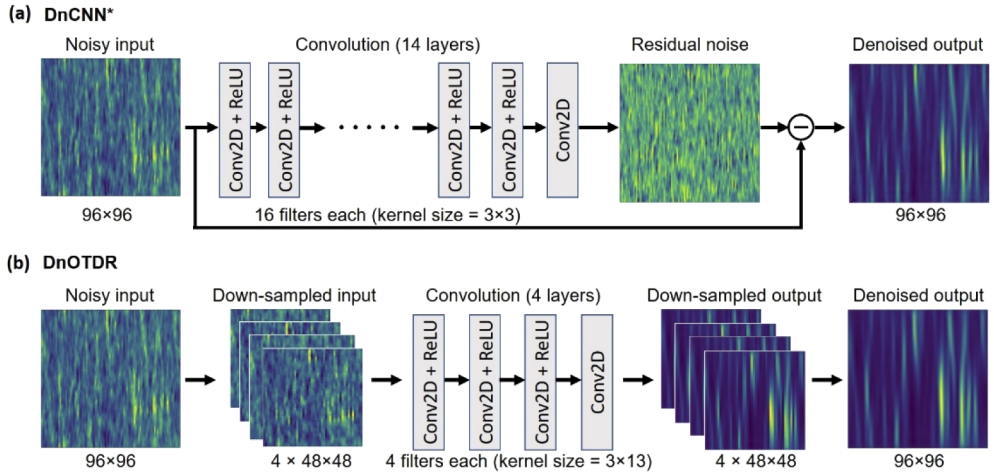

Fig. 4. Depiction of (a) DnCNN* architecture, and (b) DnOTDR architecture.

DnCNN* is a reduced version of DnCNN. The size and computation time of the model has been reduced by using only 14 convolutional layers, 16 filters, and omitting batch normalization layers without significant drop in denoising performance.

DnOTDR is a relatively shallow architecture. The first layer down-samples the 96×96 input image into four sub-images of dimension 48×48 (neighboring pixels are re-arranged into sub-images). After only four consecutive convolutional layers with only four filters each with ReLU activation, up-sampling of the sub-images to the input shape of 96×96 is conducted. The shape

Optics EXPRESS

of the kernels was adapted and optimized to three by thirteen to match the predominant shape and orientation of the backscatter structures. Increasing the number of convolutional layers or filters at the cost of computational efficiency did not considerably increase the performance.

The training of both architectures was conducted with the same training dataset. As mentioned above, the denoising performance was not validated in relation to direct output-to-ground truth comparison, but with respect to the strain results computed from the denoised output. All hyperparameter tuning was therefore based on the evaluation of the strain results from the validation dataset with the aim to minimize the strain ASD noise and accurate strain amplitude results, see Fig. 3(b). To monitor the training progress with respect to the strain results, this validation procedure was conducted after each training epoch. All model hyperparameters and training parameters were tuned to maximize the resulting strain accuracy of the validation data. This way, the two final model architectures DnCNN*, and DnOTDR, as well as specific model parameters were found. Exploring the training parameter showed minimal improvement of NPCC over MSE loss function. The learning rate was tuned to 0.0001, the training batch size to 16, and the noise factor was set to 4.5. The performance of the final trained models on the test dataset is summarized in the following section.

4. Results

The models with the best performance on the validation dataset were tested on the raw test dataset measured at $z_0 = \{60\text{ km}, 70\text{ km}, 80\text{ km}, 90\text{ km}, 100\text{ km}\}$ during a 67 nε modulation. Strain predictions were analyzed on raw data, and denoised test data using BM3D, DnCNN*, and DnOTDR. Figure 5 shows examples of single noisy test data images (left column) sampled at z_0, and denoised results of BM3D, DnCNN*, and DnOTDR in the other columns.

The visual impression is that the BM3D method fails to restore the fainter backscatter structures in the image. The much smaller and faster DnOTDR model with only 2512 trainable parameters seems to preserve details to a comparable extend as the results of the bigger and deeper DnCNN* model with 32785 trainable parameters.

Following, the strain results that were computed from denoised data using ANNs [15] are evaluated. The resulting strain distribution over distance and time is exemplarily shown at $z_0 = 100$ km for strain results computed from raw test data in Fig. 6(a), and from denoised results using DnOTDR in Fig. 6(b). Figure 6(c) and Fig. 6(d) show the resulting distribution of the strain amplitude spectrum for both results, respectively.

The stain signal at 100 km cannot be recovered from the low-SNR raw data, whereas the strain modulation from denoised data is close to the actual modulation amplitude of 67 nε. All strain amplitude distributions at the modulation frequency of 1 Hz are shown in Fig. 7(a). The results are computed from raw test data and denoised test data using DnCNN* and DnOTDR. The mean strain modulation amplitudes and the mean strain ASD noise [compare ASD depiction in Fig. 3(b)] from raw data and the denoised data are shown Fig. 7(b) and Fig. 7(c), respectively.

An on average reduced strain amplitude can be observed for all results at 100 km distance. Correct quantitative strain measurement for not denoised raw data is only possible up to 80 km distance at increased strain ASD noise. It has to be noted that the ANN-based algorithm that is used to compute the strain results from the backscatter data already improves the noise tolerance by several dB in comparison to a correlation-based approach [15]. The distance range gain compared to correlation-based strain computation would therefore be significantly higher. The evaluation results from raw data and all tested denoisers are summarized in Table 1.

It can be concluded that the CNN-based denoising algorithms improve the sensor performance and distance range and clearly outperform BM3D. The much smaller DnOTDR model shows comparable performance to DnCNN* up 90 km distance and even outperforms the DnCNN* at extremely low SNR at 100 km distance. The BM3D denoiser only marginally improves the strain results compared to the raw data for very low SNR.

Optics EXPRESS

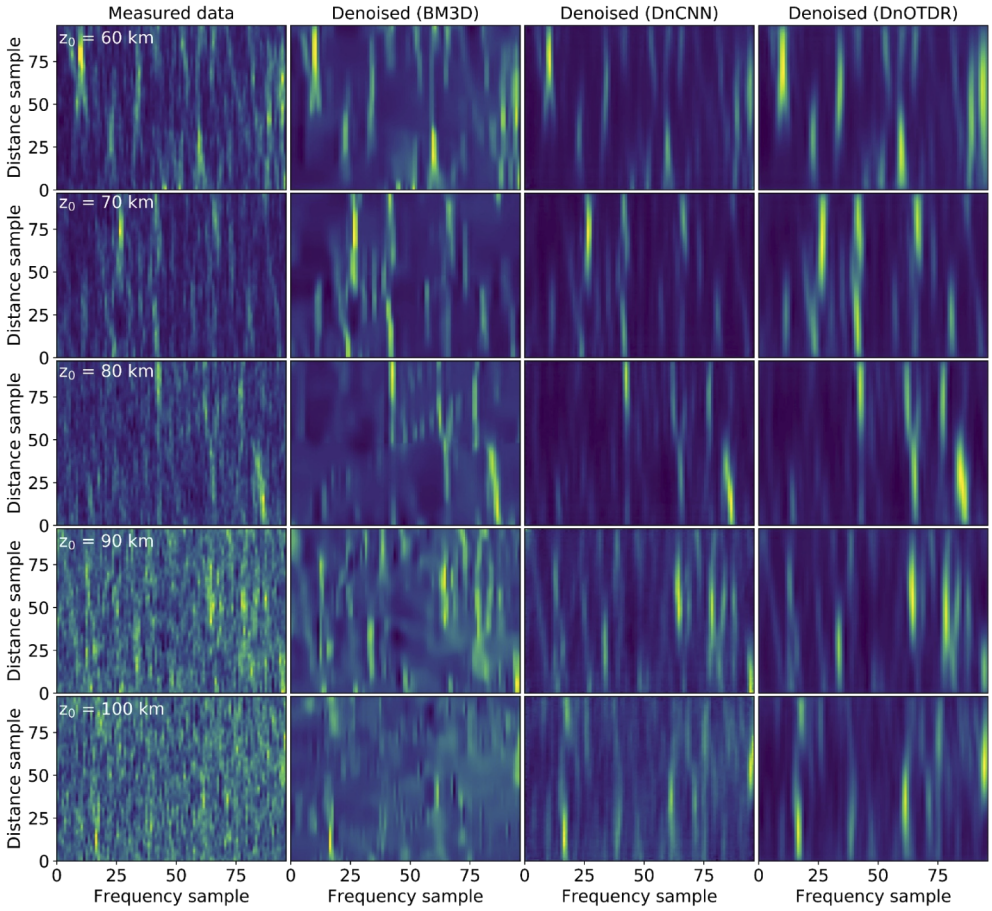

Fig. 5. Examples of raw test data and denoised data (96×96 distance samples vs. frequency samples) at different distances z_0. Row-wise: 60 km, 70 km, 80 km, 90 km, and 100 km. First column: measured raw data. The second, third and fourth column show the denoised results using BM3D, DnCNN*, and DnOTDR, respectively.

Table 1. Comparison of the sensor performance parameters strain ASD noise and peak amplitude during a 1 Hz and 67 nε amplitude modulation for low-SNR raw data and denoised data using BM3D, DnCNN*, and DnOTDR. The ASD noise from raw data and BM3D at $z_0 = 100$ km is not meaningful and is therefore omitted.

Distance z_0	Parameter	Raw data	BM3D	DnCNN*	DnOTDR
60 km	ASD noise [nε/√Hz]	0.459	0.540	0.401	0.453
	Peak amplitude [nε]	67.157	67.379	67.039	67.100
70 km	ASD noise [nε/√Hz]	0.644	0.796	0.495	0.569
	Peak amplitude [nε]	67.461	67.567	66.907	66.970
80 km	ASD noise [nε/√Hz]	1.693	1.465	0.867	0.893
	Peak amplitude [nε]	65.152	67.867	67.089	67.175
90 km	ASD noise [nε/√Hz]	4.785	4.250	1.914	2.135
	Peak amplitude [nε]	43.892	60.073	67.544	67.374
100 km	ASD noise [nε/√Hz]	-	-	5.862	5.772
	Peak amplitude [nε]	13.155	32.411	52.605	61.388

Optics EXPRESS

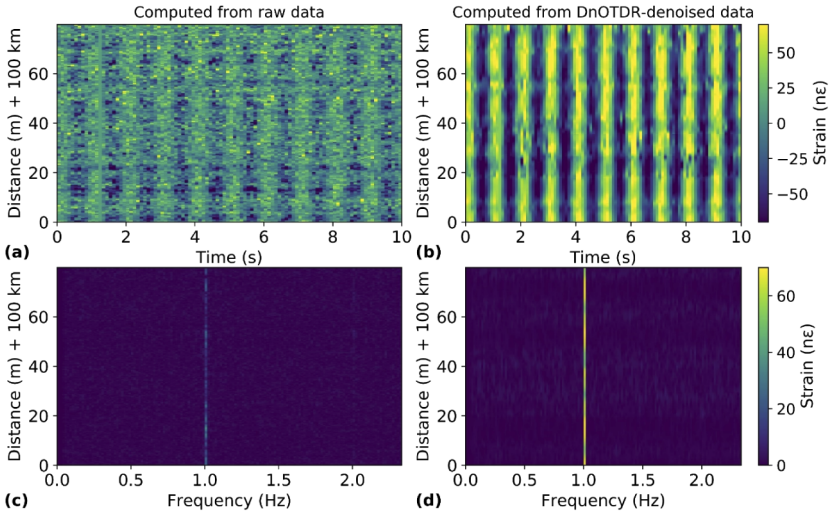

Fig. 6. Strain distribution at $z_0 = 100$ km distance during 1 Hz and 67 nε amplitude modulation: (a) computed from measured raw data, and (b) computed from the same denoised data using DnOTDR. Strain amplitude spectrum over distance computed from the same measurement over 60 s: (c) using raw data; (d) using denoised result using DnOTDR.

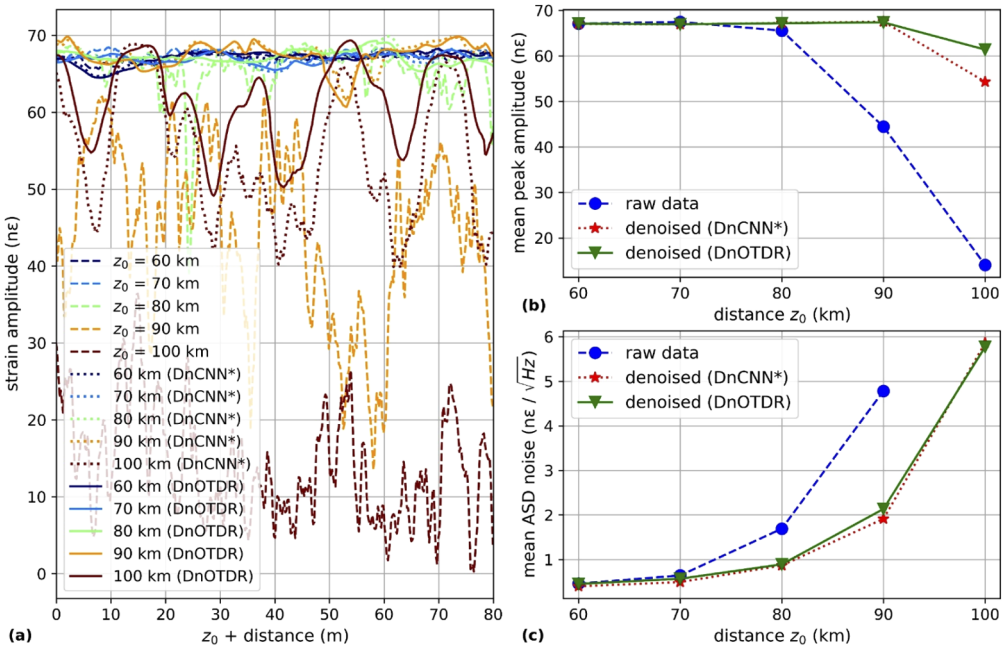

Fig. 7. (a) Strain-equivalent modulation amplitudes computed from noisy raw test data, denoised data using DnCNN*, and DnOTDR for 80 m long fiber sections at different fiber distances of $z_0 = 60$ km, 70 km, 80 km, 90 km and 100 km, respectively. (b) Mean strain amplitudes at distances z_0 computed from low-SNR raw data and denoised data. (c) Mean strain ASD noise computed from raw data and denoised data at distances z_0. (The strain ASD noise from raw data at 100 km distance is not meaningful and is therefore omitted.)

Optics EXPRESS

The most important performance parameter for real-time application is computation time. A comparison of computation times for the baseline method BM3D and the proposed DnCNN* and DnOTDR denoisers is listed in Table 2.

Table 2. Computation time for denoising per 96×96 images for DnCNN* and DnOTDR using NVIDIA RTX 2080Ti 11 GB RAM GPU, Keras v. 2.2.4, TensorFlow v. 2.2.0, and a batch size of 4000 for DnCNN* and 10000 for DnOTDR. Denoising time for BM3D implementation using CPU (16 x Intel Xeon E5-1660 v3, 3 GHz).

Denoising model	Computation time per 96×96 image	Max. data rate for real-time denoising
BM3D	1500 ms	12.3 kB/s
DnCNN[a]	0.266 ms	69 MB/s [a]
DnOTDR	0.0154 ms	1.2 GB/s [a]

[a]CNN denoising is conducted with 32-bit float resolution on the GPU. Since the data stream from the ADC is 16 bit resolution, the calculated maximum real-time data rates is based on the actual 16 bit resolution input. Real-time denoising of a 32-bit resolution 2D data stream could be conducted with the same models at twice the data rate (138 MB/s for DnCNN* and 2.4 GB/s for DnOTDR).

The CNN-based denoising models are orders of magnitude faster than the BM3D block matching algorithm. Although a GPU implementation of BM3D would accelerate the processing, the computation time and performance will lack far behind that of the convolutional neural network denoisers. The computation time of the DnOTDR denoiser for a single 96×96 image is only 15.4 µs. With the measurement settings and GPU used in this work, the DnOTDR model can be used as a real-time denoiser for fiber sections up to about 127.8 km length. The denoiser may, for example, be used for the last 30 km in the fiber where a performance increase is apparent, see Fig. 7(b) and Fig. 7(c). For long-distance sensing applications, the spatial sampling would typically be reduced from the 20.4 cm used in this work to about 1 m or more. The distance range for real-time denoising with this more realistic sampling resolution would be extended to 626 km using a consumer GPU.

5. Discussion

Although state-of-the-art ANN architectures can be adopted for tasks, similar to what they were originally designed for, specific domain knowledge is generally key to maximize the performance for most ANN applications. Extended knowledge about the application is required to generate representative training data, define useful loss functions, evaluation measures, and network architectures. The denoising performance of our tested models is solely evaluated with respect to strain ASD noise and accurate modulation amplitude. PSNR, perception-based image quality metrics, or temporal consistency of the backscatter structures are not relevant for this task. Other denoisers may perform better for lower noise levels or with respect to other performance parameters. The main goal, however, was to restore significant backscatter signatures in the presence of extremely high noise with real-time compatible computation times. The DnOTDR architecture is the only denoiser that fulfills both requirements.

Two main reasons may enable the combination of high denoising performance of the DnOTDR denoiser and very low computation time (inference time): One reason for the high performance of this compact architecture may be the limited pattern variety of the images and prevailing shape, size, and orientation of the Rayleigh backscatter structures in the distance-frequency dimension. Hence, only a small number of filters (four filters in each DnOTDR convolutional layer) suffice to map all structural varieties of the backscatter patterns. The second reason is the combination of the down-and-up sampling layers and the use of rectangular filter shapes (3×13) to fit the predominant orientation and aspect ratio of the backscatter structures. This helped reduce the necessary depth of the DnOTDR architecture to only four convolutional layers by increasing the receptive field, and matching the receptive field to the backscatter patterns.

Optics EXPRESS

By taking the third dimension time of the measured data stream into account, temporal consistencies and strain noise should theoretically be further improved. The temporal pattern propagation (from frame to frame) has been addressed in more recent CNN video denoising algorithms. We also tested various CNN-based architectures and block matching algorithms that were developed for video denoising. We trained and tested various models with specifically recorded 3D backscatter sequences. However, our not comprehensive analysis did not lead to an improved performance for our specific denoising task. Our preliminary results indicate distinct but inconsistent low-pass behavior along the time dimension. This may pose a challenge for accurate measurement applications. Although low-pass behavior may lead to visually more pleasing results for video denoising, it may prevent correct strain amplitude measurement, which is crucial for most DAS applications. This is the main reason why 3D denoising algorithms have not further been studied for this task and preliminary results were only briefly mentioned in this paper. In addition, 3D denoising algorithms are typically far more computationally expensive, which would prevent real-time use for our application. Note that this is only a preliminary assessment for our specific application. Three-dimensional data processing does have significant potential for this task and similar applications.

It has to be noted that the used DnCNN* and DnOTDR models are trained to denoise input images containing structures of a specific size, orientation, and distribution. The denoising performance for 2D-Rayleigh data that is sampled with significantly deviating measurement settings would be reduced. Ideally, particular denoisers are trained for specific measurement settings, i.e., pulse duration, spatial, and spectral sampling step size. New training data can be measured within seconds and customized models can be trained in less than one minute. Various pre-trained denoising models can be stored and readily loaded for specific measurement settings.

6. Conclusion

We demonstrated that deep convolutional neural networks can be a powerful algorithm for specific denoising tasks. Using the DnOTDR denoiser, the distance range for quantitative distributed vibration sensing was extended to 100 km and the optical return backscatter loss budget for strain measurement can be increased to about 33 dB (backscatter loss at 100 km distance). We explored the maximum distance range that could be gained by using only raw-data signal processing. Using special backscatter-enhanced fibers would extend the distance range by tens of kilometers. The use of Raman and/or Brillouin optical amplification would further extend the distance range and improve the strain noise by an even higher margin. The most significant advancement is the high denoising performance and that this can be achieved with very little computational expense. About 1.2 GB/s of 16-bit image data (2.4 GB/s with 32-bit resolution) can be denoised with a consumer GPU. This is prerequisite for real-time processing in data-intensive applications such as distributed acoustic sensing.

Funding

Bundesministerium für Bildung und Forschung (03EK3531).

Disclosures

The authors declare that there are no conflicts of interest.

References

1. A. H. Hartog, *An Introduction to Distributed Optical Fibre Sensors* (CRC, 2017, Chap. 9).
2. Y. Muanenda, "Recent advances in distributed acoustic sensing based on phase-sensitive optical time domain reflectometry," J. Sens. **2018**, 1–10 (2018).

Optics EXPRESS

3. K. Hicke, R. Eisermann, and S. Chruscicki, "Enhanced distributed fiber optic vibration sensing and simultaneous temperature gradient sensing using traditional C-OTDR and structured fiber with scattering dots," Sensors **19**(19), 4114 (2019).
4. H. F. Martins, S. Martín-López, P. Corredera, M. L. Filograno, O. Frazão, and M. Gonzalez-Herráez, "Phase-sensitive optical time domain reflectometer assisted by first-order Raman amplification for distributed vibration sensing over >100 km," J. Lightwave Technol. **32**(8), 1510–1518 (2014).
5. Z. N. Wang, J. J. Zeng, J. Li, M. Q. Fan, H. Wu, F. Peng, L. Zhang, Y. Zhou, and Y. J. Rao, "Ultra-long phase-sensitive OTDR with hybrid distributed amplification," Opt. Lett. **39**(20), 5866–5869 (2014).
6. Z. N. Wang, J. Li, M. Q. Fan, L. Zhang, F. Peng, H. Wu, J. J. Zeng, Y. Zhou, and Y. J. Rao, "Phase-sensitive optical time-domain reflectometry with Brillouin amplification," Opt. Lett. **39**(15), 4313–4316 (2014).
7. L. D. van Putten, A. Masoudi, and G. Brambilla, "100-km-sensing-range single-ended distributed vibration sensor based on remotely pumped Erbium-doped fiber amplifier," Opt. Lett. **44**(24), 5925–5928 (2019).
8. P. S. Westbrook, K. S. Feder, Roy. M. Ortiz, T. Kremp, Eric. M. Monberg, H. Wu, D. A. Simoff, and S. Shenk, "Kilometer length, low loss enhanced back scattering fiber for distributed sensing," in *25th International Conference on Optical Fiber Sensors* (Optical Society of America, 2017) (2017), paper 103239Q.
9. F. Monet, S. Loranger, V. Lambin-Iezzi, A. Drouin, S. Kadoury, and R. Kashyap, "The ROGUE: a novel, noise-generated random grating," Opt. Express **27**(10), 13895–13909 (2019).
10. G. Cedilnik, G. Lees, P. E. Schmidt, S. Herstrøm, and T. Geisler, "Pushing the reach of fiber distributed acoustic sensing to 125 km without the use of amplification," IEEE Sens. Lett. **3**(3), 1–4 (2019).
11. B. Redding, M. J. Murray, A. Donko, M. Beresna, A. Masoudi, and G. Brambilla, "Low-noise distributed acoustic sensing using enhanced backscattering fiber with ultra-low-loss point reflectors," Opt. Express **28**(10), 14638–14647 (2020).
12. C. Wang, Y. Shang, X.-H. Liu, C. Wang, H.-H. Yu, D.-S. Jiang, and G.-D. Peng, "Distributed OTDR-interferometric sensing network with identical ultra-weak fiber Bragg gratings," Opt. Express **23**(22), 29038–29046 (2015).
13. Y. Muanenda, S. Faralli, C. J. Oton, C. Cheng, M. Yang, and F. D. Pasquale, "Dynamic phase extraction in high-SNR DAS based on UWFBGs without phase unwrapping using scalable homodyne demodulation in direct detection," Opt. Express **27**(8), 10644–10658 (2019).
14. S. Liehr, S. Münzenberger, and K. Krebber, "Wavelength-scanning coherent OTDR for dynamic high strain resolution sensing," Opt. Express **26**(8), 10573–10588 (2018).
15. S. Liehr, L. A. Jäger, C. Karapanagiotis, S. Münzenberger, and S. Kowarik, "Real-time dynamic strain sensing in optical fibers using artificial neural networks," Opt. Express **27**(5), 7405–7425 (2019).
16. B. Dong, V. Tribaldos, X. Xing, S. Byna, J. Ajo-Franklin, and K. Wu, "DASSA: Parallel DAS Data Storage and Analysis for Subsurface Event Detection," *IEEE International Parallel and Distributed Processing Symposium* (IPDPS) (2020).
17. A. D. A. Ibrahim, S. Lin, J. Xiong, J. Jiang, Y. Fu, Z. Wang, and Z. Wang, "Integrated principal component analysis denoising technique for phase-sensitive optical time domain reflectometry vibration detection," Appl. Opt. **59**(3), 669–675 (2020).
18. M. Huang, M. Salemi, Y. Chen, J. Zhao, T. J. Xia, G. A. Wellbrock, Y. Huang, G. Milione, E. Ip, P. Ji, T. Wang, and Y. Aono, "First Field Trial of Distributed Fiber Optical Sensing and High-Speed Communication Over an Operational Telecom Network," J. Lightwave Technol. **38**(1), 75–81 (2020).
19. M. A. Soto, J. A. Ramírez, and L. Thévenaz, "Intensifying the response of distributed optical fibre sensors using 2D and 3D image restoration," Nat. Commun. **7**(1), 10870 (2016).
20. Y. Meng, J. Zha, and Y. Liu, "Intensifying the SNR of BOTDA using adaptive constrained least squares filtering," Opt. Commun. **437**, 219–225 (2019).
21. Z. Qin, H. Chen, and J. Chang, "Detection performance improvement of distributed vibration sensor based on curvelet denoising method," Sensors **17**(6), 1380 (2017).
22. T. Zhu, X. Xiao, Q. He, and D. Diao, "Enhancement of SNR and spatial resolution in phi-OTDR system by using two-dimensional edge detection method," J. Lightwave Technol. **31**(17), 2851–2856 (2013).
23. H. He, L. Shao, H. Li, W. Pan, B. Luo, X. Zou, and L. Yan, "SNR enhancement in phase-sensitive OTDR with adaptive 2-D bilateral filtering algorithm," IEEE Photonics J. **9**(3), 1–10 (2017).
24. G. Barbastathis, A. Ozcan, and G. Situ, "On the use of deep learning for computational imaging," Optica **6**(8), 921–943 (2019).
25. A. K. Azad, L. Wang, N. Guo, H.-Y. Tam, and C. Lu, "Signal processing using artificial neural network for BOTDA sensor system," Opt. Express **24**(6), 6769–6782 (2016).
26. Z. Cao, N. Guo, M. Li, K. Yu, and K. Gao, "Back propagation neutral network based signal acquisition for Brillouin distributed optical fiber sensors," Opt. Express **27**(4), 4549–4561 (2019).
27. N. D. Nordin, M. S. D. Zan, and F. Abdullah, "Comparative Analysis on the Deployment of Machine Learning Algorithms in the Distributed Brillouin Optical Time Domain Analysis (BOTDA) Fiber Sensor," Photonics **7**(4), 79 (2020).
28. Y. Li and J. Wang, "Optimized neural network for temperature extraction from Brillouin scattering spectra," Opt. Fiber Technol. **58**, 102314 (2020).
29. Y. Chang, H. Wu, C. Zhao, L. Shen, S. Fu, and M. Tang, "Distributed Brillouin frequency shift extraction via a convolutional neural network," Photonics Res. **8**(5), 690–697 (2020).

Optics EXPRESS

30. B. Wang, N. Guo, L. Wang, C. Yu, and C. Lu, "Robust and Fast Temperature Extraction for Brillouin Optical Time-Domain Analyzer by Using Denoising Autoencoder-Based Deep Neural Networks," IEEE Sensors J. **20**(7), 3614–3620 (2020).
31. B. Wang, L. Wang, N. Guo, Z. Zhao, C. Yu, and C. Lu, "Deep neural networks assisted BOTDA for simultaneous temperature and strain measurement with enhanced accuracy," Opt. Express **27**(3), 2530–2543 (2019).
32. R. Ruiz-Lombera, A. Fuentes, L. Rodriguez-Cobo, J. M. Lopez-Higuera, and J. Mirapeix, "Simultaneous temperature and strain discrimination in a conventional BOTDA via artificial neural networks," J. Lightwave Technol. **36**(11), 2114–2121 (2018).
33. H. Wu, C. Zhao, R. Liao, Y. Chang, and M. Tang, "Performance enhancement of ROTDR using deep convolutional neural networks," in *26th International Conference on Optical Fiber Sensors (2018)* (Optical Society of America, 2018), paper TuE16.
34. Y. Shi, Y. Wang, L. Zhao, and Z. Fan, "An event recognition method for Φ-OTDR sensing system based on deep learning," Sensors **19**(15), 3421 (2019).
35. L. Shiloh, A. Eyal, and R. Giryes, "Efficient Processing of Distributed Acoustic Sensing Data Using a Deep Learning Approach," J. Lightwave Technol. **37**(18), 4755–4762 (2019).
36. M. Aktas, T. Akgun, M. U. Demircin, and D. Buyukaydin, "Deep learning based multi-threat classification for phase-OTDR fiber optic distributed acoustic sensing applications," Proc. SPIE **10208**, 102080G (2017).
37. J. Tejedor, J. Macias-Guarasa, H. F. Martins, J. Pastor-Graells, P. Corredera, and S. Martin-Lopez, "Machine learning methods for pipeline surveillance systems based on distributed acoustic sensing: A review," Appl. Sci. **7**(8), 841 (2017).
38. Q. Sun, Q. Li, L. Chen, J. Quan, and L. Li, "Pattern recognition based on pulse scanning imaging and convolutional neural network for vibrational events in Φ-OTDR," Optik **219**, 165205 (2020).
39. Z. Wang, S. Lou, X. Wang, S. Liang, and X. Sheng, "Multi-branch long short-time memory convolution neural network for event identification in fiber-optic distributed disturbance sensor based on φ-OTDR," Infrared Phys. Technol. **109**, 103414 (2020).
40. Y. Shi, Y. Wang, L. Wang, L. Zhao, and Z. Fan, "Multi-event classification for Φ-OTDR distributed optical fiber sensing system using deep learning and support vector machine," Optik **221**, 165373 (2020).
41. Y. Bai, J. Xing, F. Xie, S. Liu, and J. Li, "Detection and identification of external intrusion signals from 33 km optical fiber sensing system based on deep learning," Opt. Fiber Technol. **53**, 102060 (2019).
42. Z. Li, J. Zhang, M. Wang, M. Wang, Y. Zhong, and F. Peng, "Fiber distributed acoustic sensing using convolutional long short-term memory network: a field test on high-speed railway intrusion detection," Opt. Express **28**(3), 2925–2938 (2020).
43. A. L. Stork, A. F. Baird, S. A. Horne, G. Naldrett, S. Lapins, J.-M. Kendall, J. Wookey, J. P. Verdon, A. Clarke, and A. Williams, "Application of machine learning to microseismic event detection in distributed acoustic sensing data," Geophysics **85**(5), KS149–KS160 (2020).
44. G. Binder and A. Tura, "Convolutional neural networks for automated microseismic detection in downhole distributed acoustic sensing data and comparison to a surface geophone array," Geophys. Prospect. **68**(9), 2770–2782 (2020).
45. S. Kowarik, M.-T. Hussels, S. Chruscicki, S. Münzenberger, A. Lämmerhirt, P. Pohl, and M. Schubert, "Fiber Optic Train Monitoring with Distributed Acoustic Sensing: Conventional and Neural Network Data Analysis," Sensors **20**(2), 450 (2020).
46. K. Dabov, A. Foi, V. Katkovnik, and K. Egiazarian, "Image denoising by sparse 3-D transform-domain collaborative filtering," IEEE Trans. Image Process. **16**(8), 2080–2095 (2007).
47. C. Tian, L. Fei, W. Zheng, Y. Xu, W. Zuo, and C.-W. Lin, "Deep learning on image denoising: An overview," arXiv:1912.13171 [cs, eess] (2019).
48. A. Lucas, M. Iliadis, R. Molina, and A. K. Katsaggelos, "Using Deep Neural Networks for Inverse Problems in Imaging: Beyond Analytical Methods," IEEE Signal Process. Mag. **35**(1), 20–36 (2018).
49. K. Zhang, W. Zuo, Y. Chen, D. Meng, and L. Zhang, "Beyond a Gaussian denoiser: Residual learning of deep CNN for image denoising," IEEE Trans. Image Process. **26**(7), 3142–3155 (2017).
50. K. Egiazarian, M. Ponomarenko, V. Lukin, and O. Ieremeiem, "Statistical evaluation of visual quality metrics for image denoising," arXiv:1711.00693 [cs] (2017).
51. Z. Wang, A. C. Bovik, H. R. Sheikh, and E. P. Simoncelli, "Image quality assessment: from error visibility to structural similarity," IEEE Trans. Image Process. **13**(4), 600–612 (2004).
52. . "SEAFOM Measuring Sensor Performance Document – 02 (SEAFOM MSP-02) DAS Parameter Definitions and Tests," (2018).
53. K. Zhang, W. Zuo, and L. Zhang, "FFDNet: Toward a fast and flexible solution for CNN-based image denoising," IEEE Trans. Image Process. **27**(9), 4608–4622 (2018).
54. D. P. Kingma and L. J. Ba, "Adam: A method for stochastic optimization," arXiv:1412.6980 [cs.LG] (2015).
55. S. J. Reddi, S. Kale, and S. Kumar, "On the convergence of Adam and beyond," in *Proceedings of International Conference on Learning Representations* (2018).